Diamond & Related Materials 108 (2020) 107981

Contents lists available at ScienceDirect

Diamond & Related Materials

journal homepage: www.elsevier.com/locate/diamond

Graphitic carbon nitride (g-C_3N_4) decorated $ZnWO_4$ heterojunctions architecture synthesis, characterization and photocatalytic activity evaluation

V. Rathi[a], A. Panneerselvam[b,*], R. Sathiyapriya ([c]Department of Physics, Mahendra Engineering College, Namakkakal-637503, Tamilnadu, India)[c]

[a] Department of Physics, Vivekanandha College of Technology for Women, Namakkal 637205, Tamilnadu, India
[b] Department of Physics, Vivekanandha College of Engineering for Women (Autonomous), Elayampalayam, Tiruchengode-637205, Tamilnadu, India
[c] Department of Physics, Mahendra Engineering College, Namakkal 637503, Tamilnadu, India

ARTICLE INFO

Keywords:
$ZnWO_4$/g-C_3N_4
Hydrothermal
Catalyst
4-Chlorophenol
Visible light

ABSTRACT

Herein, efficient $ZnWO_4$/g-C_3N_4 hybrid photocatalysts with effective interfaces were designed by controlling the surface charges of the two individual materials via facile hydrothermal method. The photocatalysts were characterized by X-ray diffraction (XRD), Transmission electron microscopy (TEM), Energy dispersive X-ray (EDX) analysis, Raman, N_2 adsorption-desorption, Photoluminescence spectroscopy (PL) and UV–Vis diffuse reflectance spectra analysis. XRD and TEM results indicate the reasonable existence of g-C_3N_4 (001)-$ZnWO_4$ (010) interfaces. The incorporated g-C_3N_4 layer has shown a great impact on the structure and properties, including lattice expansion, band-gap narrowing, luminescence enhancement, as well as photocatalytic activity. Visible light induced photocatalytic degradation test was carried out for all the synthesized catalysts towards rhodamine B (RhB) and 4-chlorophenol (4-CP) dyes. The results reveal that the hybrid catalyst show outstanding degradation efficiency of 99%, high apparent constant (0.0931 min^{-1}) and long term stability towards RhB dye under visible light irradiation. The degradation efficiency is only ~41 and 47% for the pure g-C_3N_4 and $ZnWO_4$ catalysts, respectively. The synergic effect between these hybrid materials photocatalytic mechanism was also discussed in brief.

1. Introduction

In the past decades, great progress has been made in the development of semiconductor photocatalysis for environmental protection and health sectors [1]. Photocatalysts are expected to play important roles in solving environment problems, particularly for the removal of organic and inorganic pollutants. Semiconductor photocatalysts films have attracted widespread interest as promising materials for the removal of organic contaminants. Nevertheless, TiO_2 is one of the most widely used photocatalysts, suffers from two main problems, which are the lows solar energy conversion efficiency and the high recombination of photo-generated electron–hole pairs. Therefore, great efforts have been devoted to searching for new efficient photocatalysts [2–11]. Since, it represents an easy way to utilize the energy of either natural sunlight or artificial indoor light, which is inexhaustibly accessible all over in the world. In any case, most of the broadly utilized photocatalysts have two primary restrictions: one is the low solar energy conversion proficiency due to their wide band gap, and the other is the high recombination ratio of photo-induced electron-hole pairs. In this regard, looking for exceedingly dynamic photocatalysts is still a growing effort around the world. Currently, inorganic nanostructured materials have paid much attention in energy and environmental applications [12]. Among them, metal tungstates (AWO_4; A = Cu, Mn, Zn, Co, Ni, Sm, etc.) were broadly utilized in different potential applications due to their extraordinary physicochemical properties [13].

In particular, zinc tungstate ($ZnWO_4$), the 6- fold facilitated ZnO_6 and WO_6 octahedrons are associated by means of corner sharing of oxygen atoms [14]. The compound shows self-activated luminescence and great photocatalytic capability, both emerging from its photoactive tungstate ligand [15], and has generally stable electrochemical properties, high refractive index, short fluorescence decay and non-toxicity [16]. It has widely used in numerous important applications including

* Corresponding author. Department of Physics, Vivekanandha College of Engineering for Women (Autonomous), Elayampalayam, Tiruchengode-637205, Tamilnadu, India,
E-mail address: panneer.phy@gmail.com (A. Panneerselvam).

https://doi.org/10.1016/j.diamond.2020.107981
Received 18 May 2020; Received in revised form 12 June 2020; Accepted 17 June 2020
Available online 30 June 2020
0925-9635/ © 2020 Elsevier B.V. All rights reserved.

gas sensor, humidity sensor, solid state laser host, optical fibers, LED, catalysis and photocatalysis areas [17]. However, because of its high recombination ratios of photo-generated electron–hole pairs, the degradation efficiency of phenol is relatively low. In order to address these issues, coupling of heterojunction photocatalyst, which is consists with combination of metal oxides with carbonaceous based materials (Reduced graphene oxide, graphene, CNT and g-C_3N_4 etc.), is the effective way to improve the photocatalytic performance [18]. Recently, graphitic carbon nitrides (g-C_3N_4) are considered as a promising candidate for preparation of hetero-nanostructure photocatalysts [19–23]. It is a soft polymer so that it can easily coat on other compounds surface. On the other hand, its graphene like sp^2 bonding structure, together with abundant in-plane nitrogen dopants and defects, gives it an appealing electronic structure [24], which is responsible for its multifunctional catalytic activity [25]. Compared with other photocatalysts, g-C_3N_4 combines the advantages of low cost, non-toxicity and visible light activity. For example, Wang et al. have reported the synthesis of RGO-$ZnWO_4$ nanocomposite for photocatalysis applications and decomposition of various toxic pollutants under visible light irradiation [26] and his groups was further designed the ternary photocatalyst, which is combination with RGO-$ZnWO_4$-Fe_3O_4 nanocomposite for visible light photocatalysis. The results illustrate that the ternary photocatalyst show outstanding degradation efficiency towards various organic pollutants under visible light illumination [27–29]. L. Sun et al. [30] reported systematic investigation of the microscopic mechanism of interface interaction, charge transfer and separation, as well as their influence on the photocatalytic activity of heterojunctions by a combination of theoretical calculations and experimental techniques for the g-C_3N_4–$ZnWO_4$ composite. In this report, the desired $ZnWO_4$/g-C_3N_4 heterojunction photocatalysts were synthesized by hydrothermal method. The hydrothermal method is a promising liquid phase preparation technology that has developed rapidly during recent years. It is widely used in many fields, such as the piezoelectric, ferroelectric, ceramic powder, and oxide film fields. The hydrothermal method has resulted in many new methods during the long-term research process, such as adding other force fields to the hydrothermal condition reaction system. These force fields mainly include direct current, electric, magnetic (autoclaves composed of non-ferroelectric materials), and microwave fields. In addition, the crystal size, morphology, and agglomeration of ceramic oxides can be controlled by adjusting the ratio of starting materials, pH of the reaction system, time, and temperature of the reaction. Moreover, the method is convenient operation, simple synthesis process, and controllable particle size. The photocatalytic experimental results showed that, under visible-light illumination, the hybrid composite catalyst exhibits tremendous degradation efficiency towards RhB and 4-CP dyes. The narrowing the band gap end separation of charge carrier with possible photocatalytic mechanism of the hybrid catalyst was systematically investigated.

2. Experimental procedure

2.1. Materials

Melamine ($C_3H_6N_6$, 99%) was used in this study as a carbon nitride precursor. Sodium tungstate (Na_2WO_4), zinc nitrate dihydrate (Zn $(NO_3)_3{\cdot}2H_2O$), sodium hydroxide (NaOH), rhodamine B (RhB) and 4-Chlorophenol (4-CP) solutions were purchased from Alfa Aesar company (Japan) with purity of 99%. Chemicals were used any further sanitization.

2.2. Preparation of g-C_3N_4, $ZnWO_4$ and $ZnWO_4$/g-C_3N_4 nanocomposites

Bare g-C_3N_4 was synthesized from Melamine, which is direct annealing of 450 °C for 2 h in air environment [31]. In this process, 2 g melamine was put into an alumina crucible with a cover and calcined at 450 °C, with a heating rate of 2 °C min^{-1}, then kept for 2 h at this temperature. Finally, the coarse g-C_3N_4 was grinded into the powder before further characterization. A facile hydrothermal route was used to prepare the $ZnWO_4$ nanoparticles. Initially, 1.65 g of Na_2WO_4 and 0.85 g of $Zn(NO_3)_3{\cdot}2H_2O$ were mixed with 50 ml of DI water under vigorous stirring of 30 min. Subsequently, the concentrated NaOH solution was added into the above solution to adjusting the pH value to reaches to 8. When NaOH is added in the precursor solution, it mixed well with the precursor solution and increased the pH of the solution. NaOH absorbs more hydrothermal reaction than ammonia which results in increased reaction rate. The pH value was found to 6.5 before adding of NaOH. The resultant suspension was transferred into a Teflon-lined stainless steel autoclave and heated to 150 °C and kept for 12 h, and then cooled down naturally. The milky white gel was sequentially washed with water, ethanol, and acetone (20 mL of each) and dried in a dessicator under low vacuum (approx. 10^{-2} mbar) for 24 h and dried at 80 °C overnight. The final product is pure $ZnWO_4$ nanopowders. The g-C_3N_4/$ZnWO_4$ photocatalysts were prepared through several steps. First, an appropriate amount of g-C_3N_4 was added into methanol to be ultrasonically stirred for 1 h to completely disperse the g-C_3N_4. Then, the $ZnWO_4$ power was added into the g-C_3N_4 suspension and magnetically stirred in a fume hood until solvent evaporation was completed. The g-C_3N_4/$ZnWO_4$ composite photocatalysts with different g-C_3N_4 mass ratios were obtained after drying at 80 °C and then calcinating at 300 °C for 4 h to provide enough thermal energy to achieve an interaction between $ZnWO_4$ and g-C_3N_4 samples, which could provide a favorable condition for charge transfer from one particle to the other via the interfaces. The mass ratios of the resulting samples were as follows: g-C_3N_4: $ZnWO_4$ = 1:1, 2:1, and 3:1. The composites with these different mass ratios were denoted here as ZWG1, ZWG2 and ZWG3, respectively.

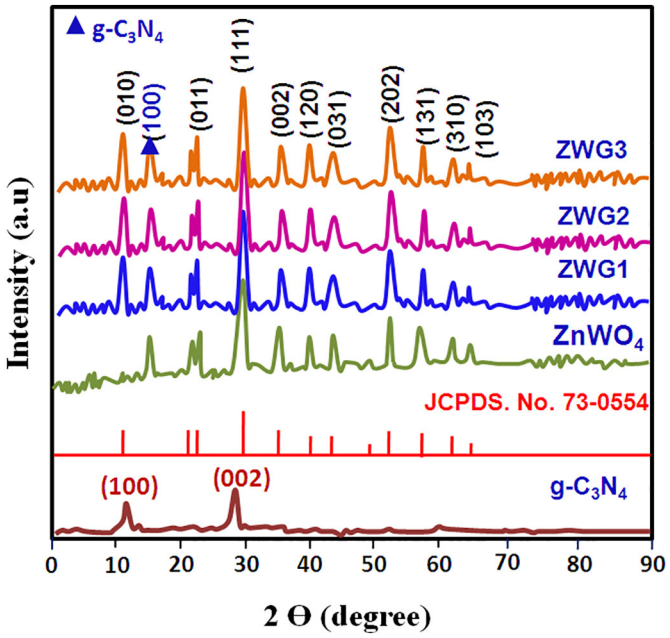


Fig. 1. Powder X-ray diffraction pattern of pure g-C_3N_4, $ZnWO_4$ and various composite samples.

2.3. Characterization techniques

Bruker D8 diffractometer with Cu Kα radiation (λ = 1.5418 Å) was used to analysis the structural nature of the samples. The microstructure and elemental composition of the samples were analyzed by using scanning electron microscope (JEOL Model JSM - 6390LV), transmission electron microscope (TEM, H-600-II, Hitachi) and energy dispersive spectra (EDS) (JEOL Model JED – 2300) analysis. The

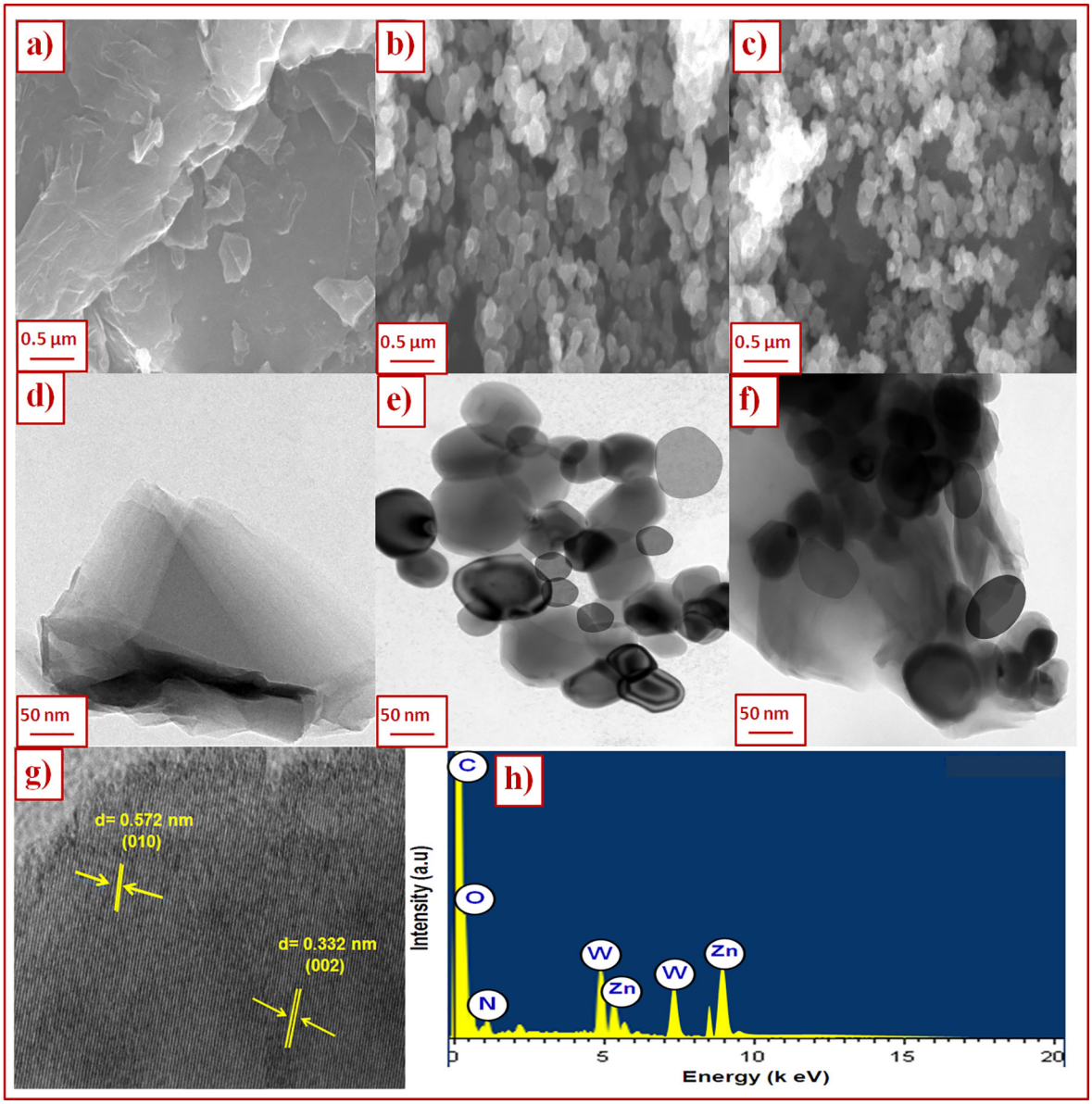


Fig. 2. SEM images of a) g-C_3N_4; b) $BiVO_4$; c) ZWG3; TEM images of d) g-C_3N_4; e) $ZnWO_4$; e) ZWG3; f) EDAX spectra of BVG3.

fundamental vibration modes of the samples were measured by Fourier transforms infrared spectroscopy (FT-IR, Nicolet Nexus 470). The photoluminescence (PL) spectra of the samples were obtained by a QuantaMaster & TimeMaster Spectrofluorometer with an excitation wavelength at 38 nm using He-Ne laser as input source. The specific surface areas and porous nature of materials were further investigated by nitrogen adsorption/desorption measurements on nova 2200e. BRUKER RFS 27: spectrometer and Perkin- Elmer lambda 950 UV–vis.-NIR spectrophotometer was utilized to identify the vibration mode and optical nature of the products.

2.4. Photocatalytic assembly

A glass type photo-reactor which is consists of 500 ml capacity with dimension of 15 cm diameter and 20 cm height. Xenon lamp XQ-500 W with an intensity of 40 mW/cm^2 has been used as the source of visible light to activate the photocatalytic reaction. Initial concentration of the solution consists of 10 mg of catalyst powders with mixed with 50 ml of dyes (20 mg L^{-1}) and stirred for about 30 min to accomplish the adsorption-desorption equilibrium. The absorption ability of rhodamine B (RhB) and 4-chlorophenol (4-CP) dyes were monitored using UV–Vis-NIR spectrophotometer (UV-2600SHIMADZU) with the corresponding wavelength of 540 and 220 nm, respectively. The visible light activation time is varied from 0 to 100 min with optimum interval of 20 min. The photocatalytic degradation efficiency (E) was obtained by the following formula [32,33]:

$$E = (1 - C/C_0) \times 100\% = (1\text{–}A/A_0) \times 100\%$$

where C is the concentration of the solution at reaction time t, C_0 is the adsorption/desorption equilibrium concentration at reaction time t0, A and A_0 are the corresponding values.

3. Results and discussion

3.1. Powder X-ray diffraction (XRD) analysis

XRD measurement was recorded to identify the information of crystallographic nature and purity of the samples. Fig. 1 shows the XRD graph of pristine g-C_3N_4, $ZnWO_4$ and various compositions of the catalyst samples. There are two peaks of g-C_3N_4 is located at 11.2° and

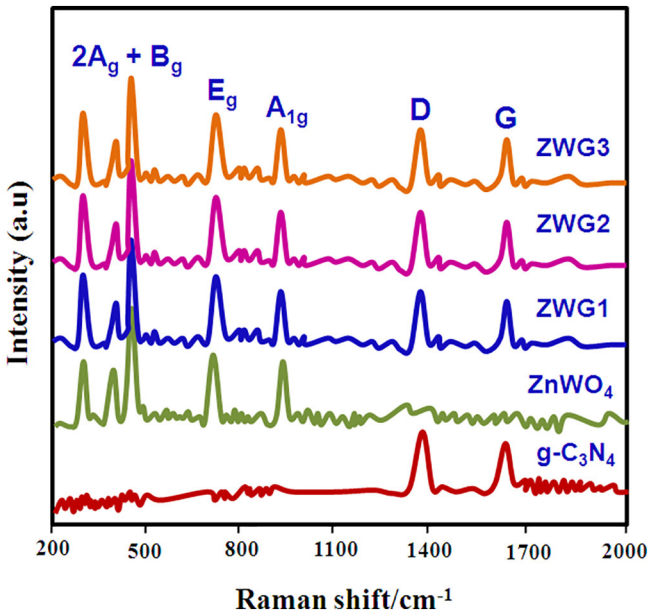


Fig. 3. FTIR spectra of pure g-C_3N_4, $ZnWO_4$ and various composite samples.

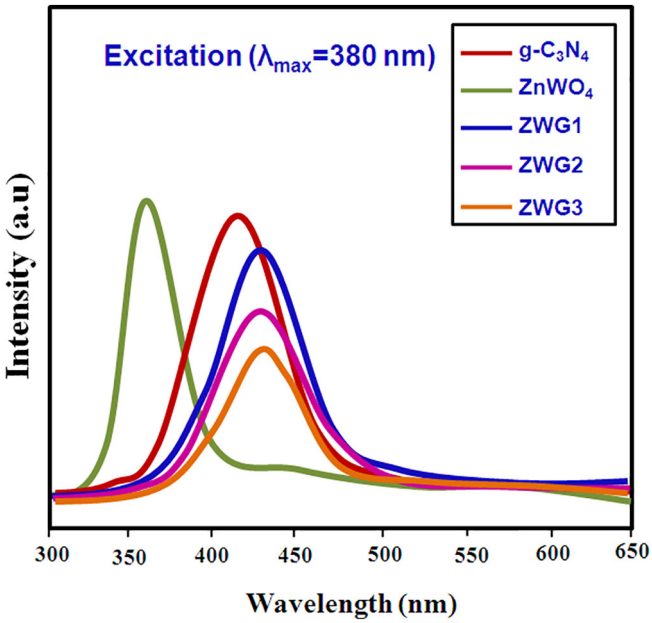


Fig. 5. Photoluminescence spectra of pure g-C_3N_4, $ZnWO_4$ and various composite samples.

27.8° equivalent to 0.288 nm and 0.335 nm can be allocated to (100) and (002) facet [34]. Pure $ZnWO_4$ show a series of diffraction angles at 15.35, 23.73, 24.38, 30.65, and 36.42°, corresponded to 0.571, 0.372, 0.364, 0.293, and 0.243 nm, which can be assigned to (010), (01 1), (021), (111), (002). All the diffraction peaks can be indexed to the monoclinic ZnWO4 phase structure with the space group of P2/C which is good consistence to their standard JCPDS file No. 73-0554 [35]. No peak related to g-C_3N_4 is detected in the bare $ZnWO_4$ catalyst, but all the composite catalyst show combination diffraction of both g-C_3N_4 and $ZnWO_4$. This could be due to the composition of heterojunction catalyst behavior of the samples. Further, the sharp intense peak of the composite sample is indicated that high order crystalline nature.

3.2. SEM, TEM, HRTEM with EDAX analysis

Morphological feature of the catalyst were analyzed via SEM, TEM and HRTEM images. Fig. 2(a–c) displays the SEM images of g-C_3N_4, $ZnWO_4$ and $ZnWO_4$/g-C_3N_4 (ZWG3) composite samples, respectively. The clear sheet like and mono-dispersed collective spherical shaped particles were found in the of g-C_3N_4 and $ZnWO_4$ samples. The $ZnWO_4$ nanoparticles are decorated on the g-C_3N_4 nanosheets surface, which can be found in the composite samples. The obvious sheets like with layer structure and spherical shaped morphologies were found in the TEM images (Fig. 2d&e). The uniform decoration of $ZnWO_4$ nanoparticles on the g-C_3N_4 nanosheets surface was clearly visible in the composite sample (Fig. 2f). The interaction of $ZnWO_4$ and g-C_3N_4 was further examined by HRTEM image (Fig. 2g). The clear lattice fringes of 0.572 nm and 0.332 nm indexed for (010) and (002) planes of $ZnWO_4$ and g-C_3N_4, respectively. The interface between these heterostructure is encouraging for the transport of photoexcited carriers and improved the photocatalytic activities. The corresponding EDS image is further proof to creation of heterojunction due to the presence of major elements such as N, C, O, W and Zn (Fig. 2h).

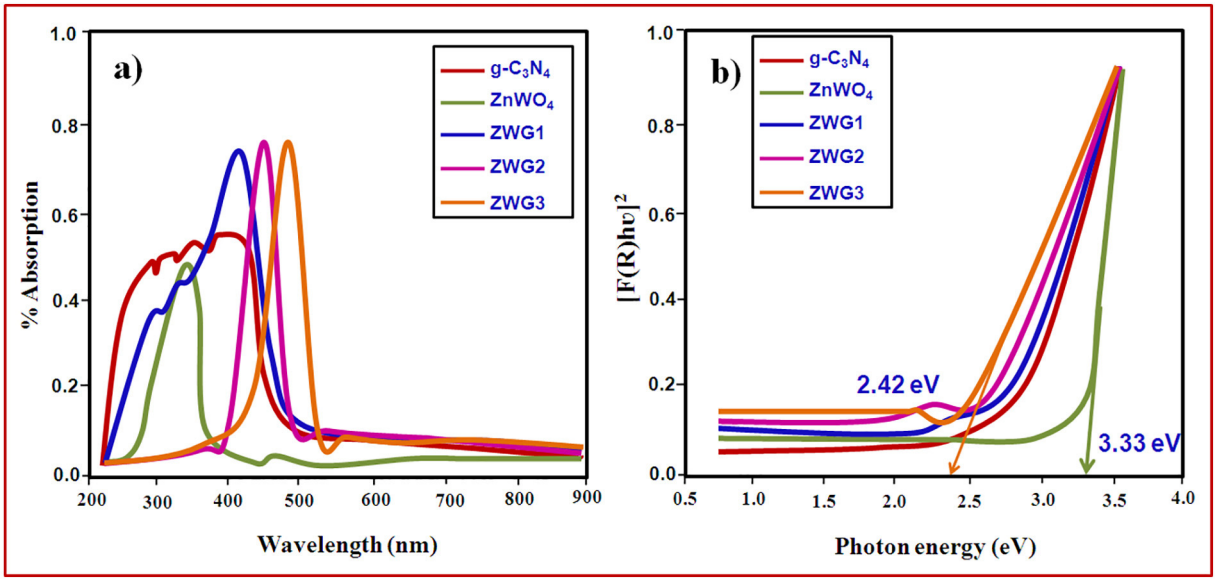


Fig. 4. UV–Vis DRS spectra of pure g-C_3N_4, $ZnWO_4$ and various composite samples. a) Absorption spectra b) Kubelka-Munk model.

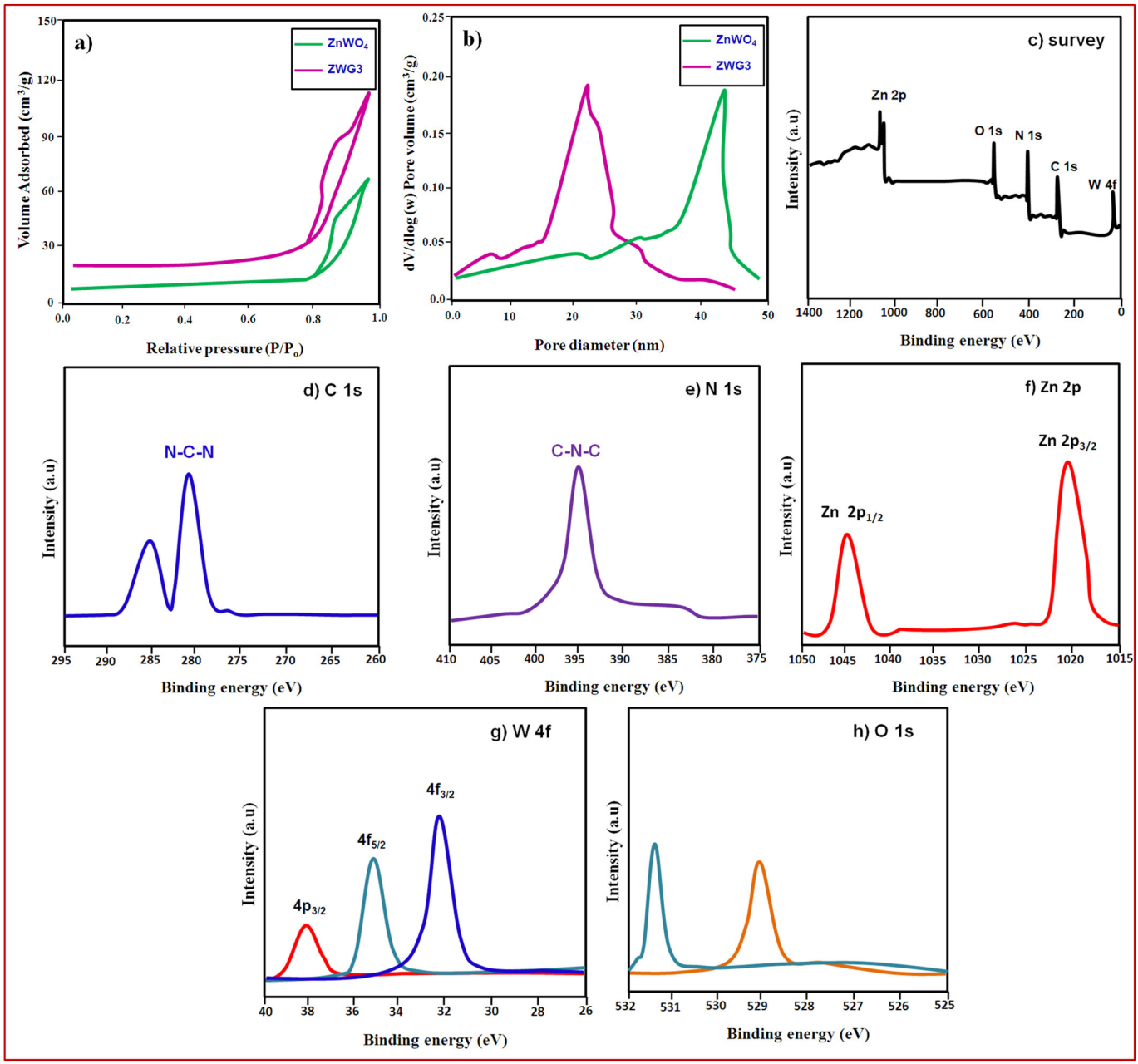


Fig. 6. a) N_2 adsorption and desorption analysis $ZnWO_4$ and ZWG3 samples. b) Corresponding pore size distribution; XPS of ZWG3 c) survey; d) C 1s; e) N 1s; f) Zn 2p; g) W 4f and h) O 1s.

3.3. Raman spectra analysis

Raman spectroscopy was also performed to better understand the interaction of g-C_3N_4 and $ZnWO_4$, and the results are displayed in Fig. 3. The obvious D and G bands were positioned at 1345 cm^{-1} and 1581 cm^{-1} in the pure g-C_3N_4 catalyst illustrate that inter-layer–stacking of aromatic systems as in g-C_3N_4 [36]. A series of Raman modes (275, 356, 415, 702 and 915 cm^{-1}) in the bare $ZnWO_4$ catalyst is due to the internal and external vibration modes of ZnO_6 octahedron and WO_6 octahedron [37]. A_{1g} symmetric stretching (~915 cm^{-1}), E_g asymmetric stretching (~702 cm^{-1}) and T_{2g} bending deformation (2Ag + Bg, ~415, 356 and 275 cm^{-1}) are corresponding to the monoclinic structure of $ZnWO_4$ [38]. The coexistence of g-C_3N_4 and $ZnWO_4$ Raman modes in the composite sample is found and the relative intensity variation also been observed. This could be due to the size variation of the different samples. The I_D/I_G ratio value of the g-C_3N_4 is calculated to be 1.15, which is higher than that of $ZnWO_4$/g-C_3N_4 (ZWG3) (0.78), indicating successful incorporation of g-C_3N_4 in the $ZnWO_4$ matrix.

3.4. UV–Vis DRS analysis

Fig. 4a) shows the UV–Vis absorption spectra of all the catalysts samples. The bare $ZnWO_4$ show the absorption edge in the UV region (372 nm), while the absorption edge is extended in the visible light region (450 nm) for g-C_3N_4 catalyst. Due to the synergic interactions of g-C_3N_4 and $ZnWO_4$ in the composite, the absorption edge was significantly shifted towards the higher angle side. The results suggest that the visible light absorption is considerably increases and narrowing the band gap energy of the samples. Moreover, the significant enhanced absorption intensity in the visible light, resulting from the role of g-C_3N_4 as a light sensitizer in the heterojunctions, is another factor for the

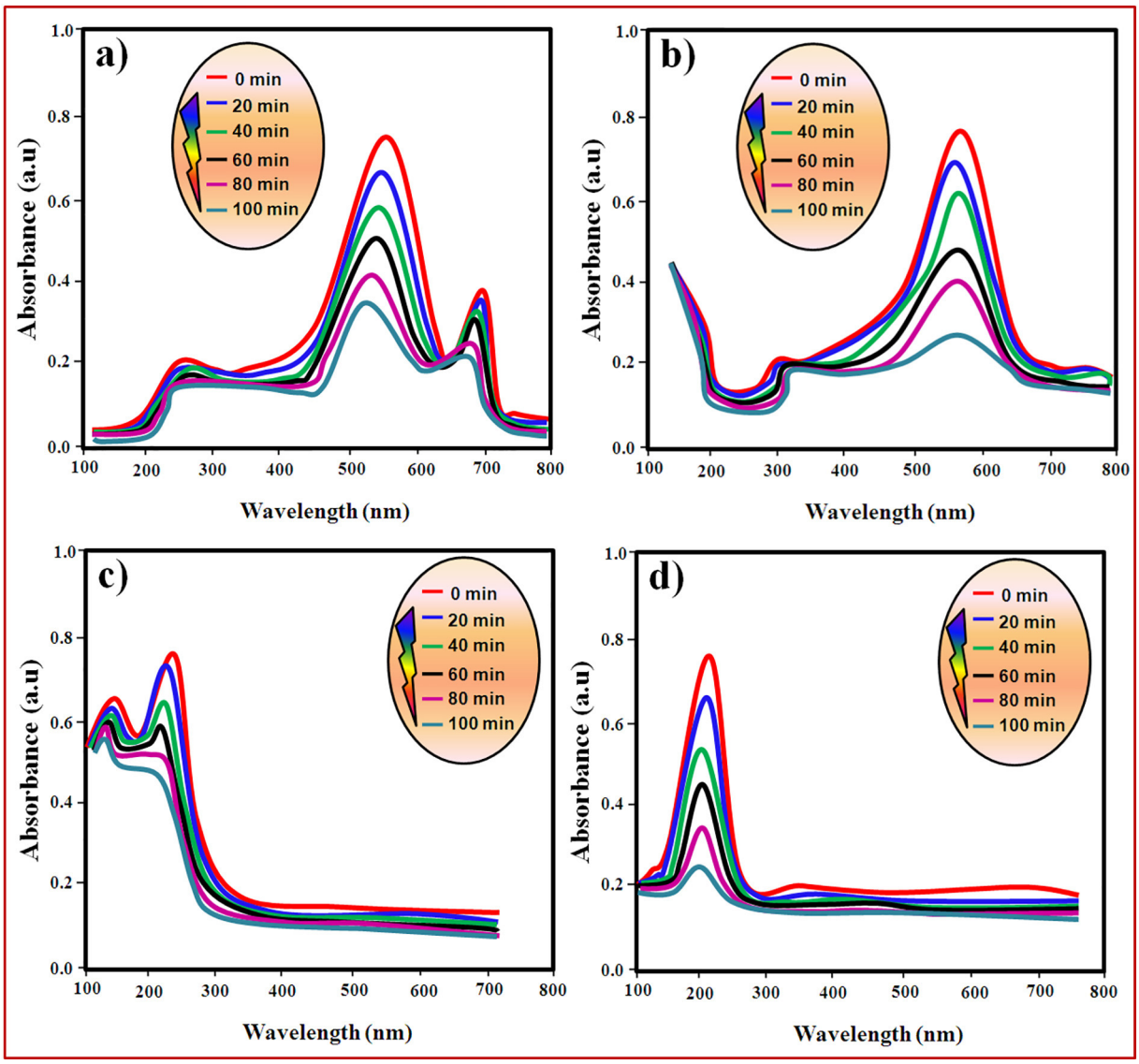


Fig. 7. UV absorption spectra of RhB using a) $ZnWO_4$; b) ZWG3; UV absorption spectra of 4-CP using c) $ZnWO_4$; d) ZWG3 under different illumination time.

improved visible-light photocatalytic activity of as-prepared heterojunctions. The band gap energies calculated using Kubelka – Munk (K-M) model [39] is described below; $K/S = (1- R_\infty)^2/2R_\infty = F(R_\infty)$. The K-M model at any wavelength is given by $F(R_\infty)$ is the so called remission or Kubelka – Munk function, where R_∞ = R sample/R standard where R is the percentage of reflectance. A graph is plotted between $[F(R_\infty)h\upsilon]^2$ Vs hυ and the intercept value is the direct band gap energy [40]. The extrapolated band gap energies are 2.75, 3.33, 2.68, 2.53 and 2.42 eV for g-C_3N_4, $ZnWO_4$, ZWG1, ZWG2 and ZWG3 catalysts, respectively (Fig. 4b).

3.5. Photoluminescence spectra analysis

Structural disorder or defects and photo-induced electron-hole pair recombination rate of the semiconducting nanoparticles are generally evaluated using the photoluminescence studies. The measurement of PL emission is often carried out on many kinds of photocells because it is a natural recombination process competitive to the required separation and photocurrent generation. The goal is to reduce the emission intensity in the photoluminescence as much as possible. Fig. 5 shows the room temperature PL spectra of all the catalysts measured with the wavelength region of 350–650 nm. He-Ne with excitation wavelength of 380 nm has been used to trigger the luminescence properties. The emission intensity of g-C_3N_4 and $ZnWO_4$ catalysts were found to be 440 and 360 nm. While, the emission intensity was significantly shifted towards the longer wavelength side. A considerable red-shift in the emission intensity of composite sample sis due to effective generation of electron-hole pair. It was clearly seen that the emission intensity was drastically decreased when the g-C_3N_4 content is increased in to the $ZnWO_4$. Hence, the PL results suggest that a drastic decrease in emission intensity was observed in the composite sample than compared with pure samples. This might be attributed to prevent the recombination rate of electron-hole pair, which is encouraging for developing the photocatalytic efficiency.

3.6. Nitrogen adsorption and desorption analysis

The specific surface area and pore size distribution was performed by the N_2adsorption/desorption analysis (Fig. 6a) and estimated via Brunauer–Emmett–Teller (BET) Barrett- Joyner-Halenda (BJH) model (Fig. 6b). The curve clearly displays a type IV isotherm with H3 type hysteresis loop, indicating that mesoporous nature of the samples [41,42]. The BET surface area and BJH pore size was found to be 94.8 m^2/g and 22.51 nm for NWG3 catalyst, which is higher than bare

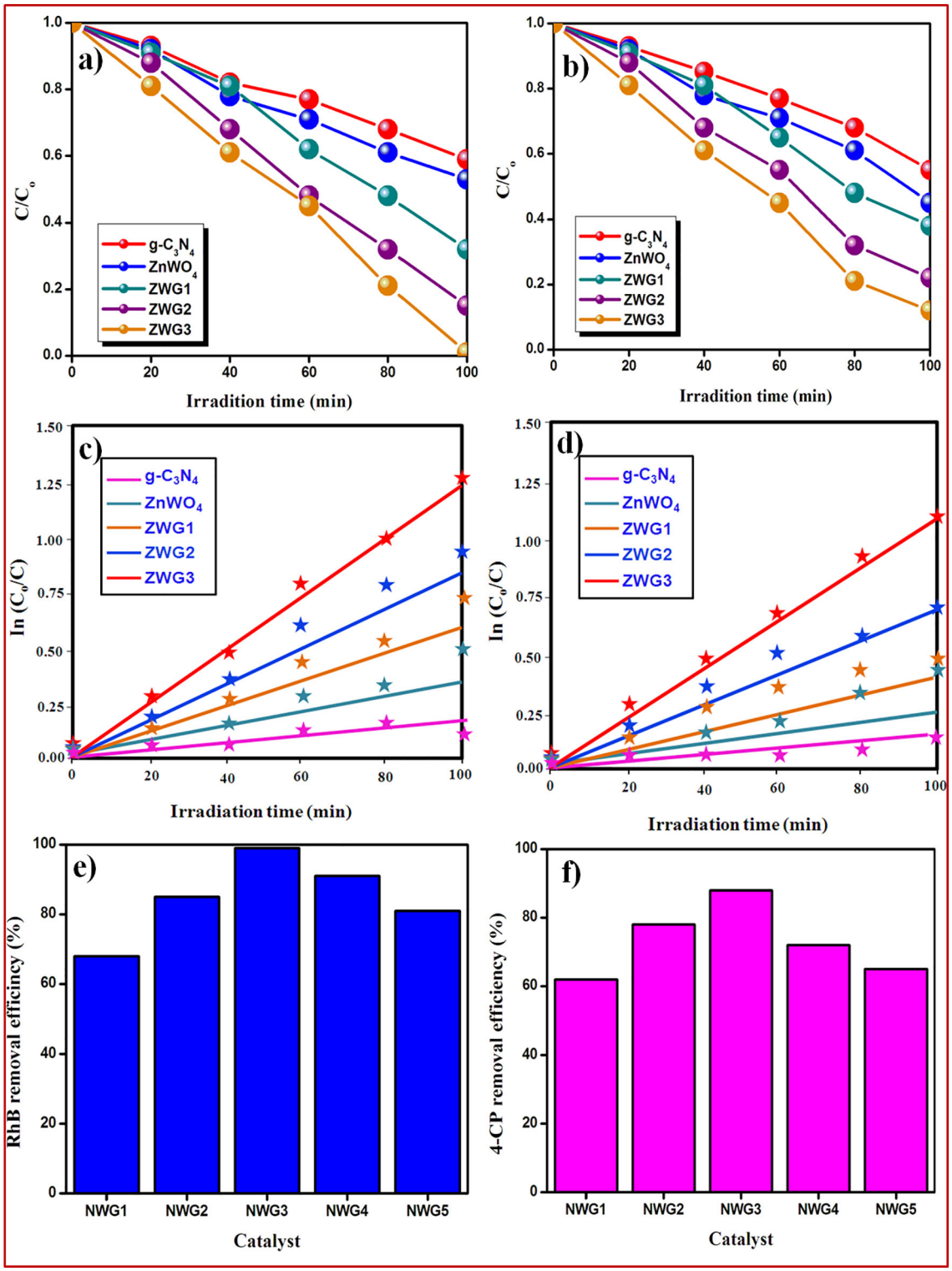


Fig. 8. Temporal degradation profile of a) RhB; b) 4-CP; Kinetic plot of c) RhB; d) 4-CP for all the catalyst powders; effect of catalysts dosage on the degradation efficiency of e) RhB; f) 4-CP.

$NiWO_4$ catalyst (56.8 m^2/g and 43.67 nm). The improved textural properties of the composite sample is due to the interface between the g-C_3N_4 and $ZnWO_4$ heterojunctions, which might be promote adsorption, desorption, and diffusion of reactants and products, which was favorable to the photocatalytic performance.

3.7. XPS analysis

The chemical composition and valance state of the sample was further examined by XPS. Fig. 6c) shows the survey spectrum of $ZnWO_4$/g-C_3N_4 (ZWG3) sample, which is mainly composed of Zn, W, O, C and N. From Fig. 6(d), the peak of C 1 s binding energies at 284.1 eV can be ascribed to the adventitious carbon species in g-C_3N_4. The peak

Table 1
Photocatalytic parameters of pure g-C_3N_4, $ZnWO_4$ and various composite samples.

Samples	Band gap (eV)	Rate constant of RhB		Rate constant of 4-CP		Degradation efficiency at 100 min	
		K (h^{-1})	R^2	K (h^{-1})	R^2	RhB	4-CP
g-C_3N_4	2.75	0.0012	0.965	0.0112	0.965	41	45
$ZnWO_4$	3.33	0.0221	0.948	0.0171	0.974	47	55
ZWG1	2.68	0.0451	0.933	0.0231	0.945	68	62
ZWG2	2.53	0.0621	0.988	0.0452	0.971	78	78
ZWG3	2.42	0.0931	0.994	0.0721	0.984	99	88

located at 288.1 eV can be assigned to sp2-bonded carbon in N-containing aromatic rings (N-C-N), which are the major carbon species in the g-C_3N_4. The peak of N 1s binding energies at 395.1 eV can be ascribed to the sp2 hybridized aromatic nitrogen atoms bonded to carbon atoms (C-N-C) [43,44] (Fig. 6(e)). The binding energy values of Zn $2p_{3/2}$ and Zn $2p_{1/2}$ are observed at 1021.5 and 1045.2 eV, respectively, which can be assigned to the Zn^{2+} ions of the $ZnWO_4$ [] (Fig. 6(f)). The high resolution spectra of the W4f exhibits three peaks with binding energies are 32.5, 35.1 and 38.1 eV (Fig. 6(g)). The O 1s peaks were obtained at 529.1 and 531.5 eV as shown in Fig. 6(h).

3.8. Photocatalytic studies

3.8.1. UV absorption characteristics

The photocatalytic performances of the all the catalysts were studied through absorption ability, removal efficiency, kinetic reaction and stability test of RhB and 4-CP pollutants under visible light irradiation. The absorption ability of the catalysts towards RhB and 4-CP dyes were initially monitored under various illumination time of visible light and the resultant plot is shown in Fig. 7(a–d). Absorption ability of the catalysts was evaluated using RhB and 4-CP dyes with equivalent wavelength of 540 and 220 nm, respectively. UV–Vis-NIR spectrophotometer (UV-2600SHIMADZU) was carried out to monitor the absorption characteristics of the catalysts. The strong absorption intensity was found with respective dyes with equivalent wavelength region at absence of visible light. When the visible light illumination is increases

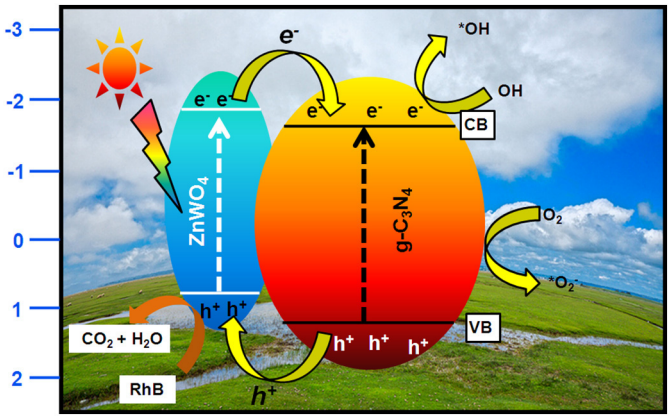


Fig. 10. Schematic representation of the photocatalytic mechanism of the $ZnWO_4$/g-C_3N_4 hybrid photocatalyst under visible light irradiation.

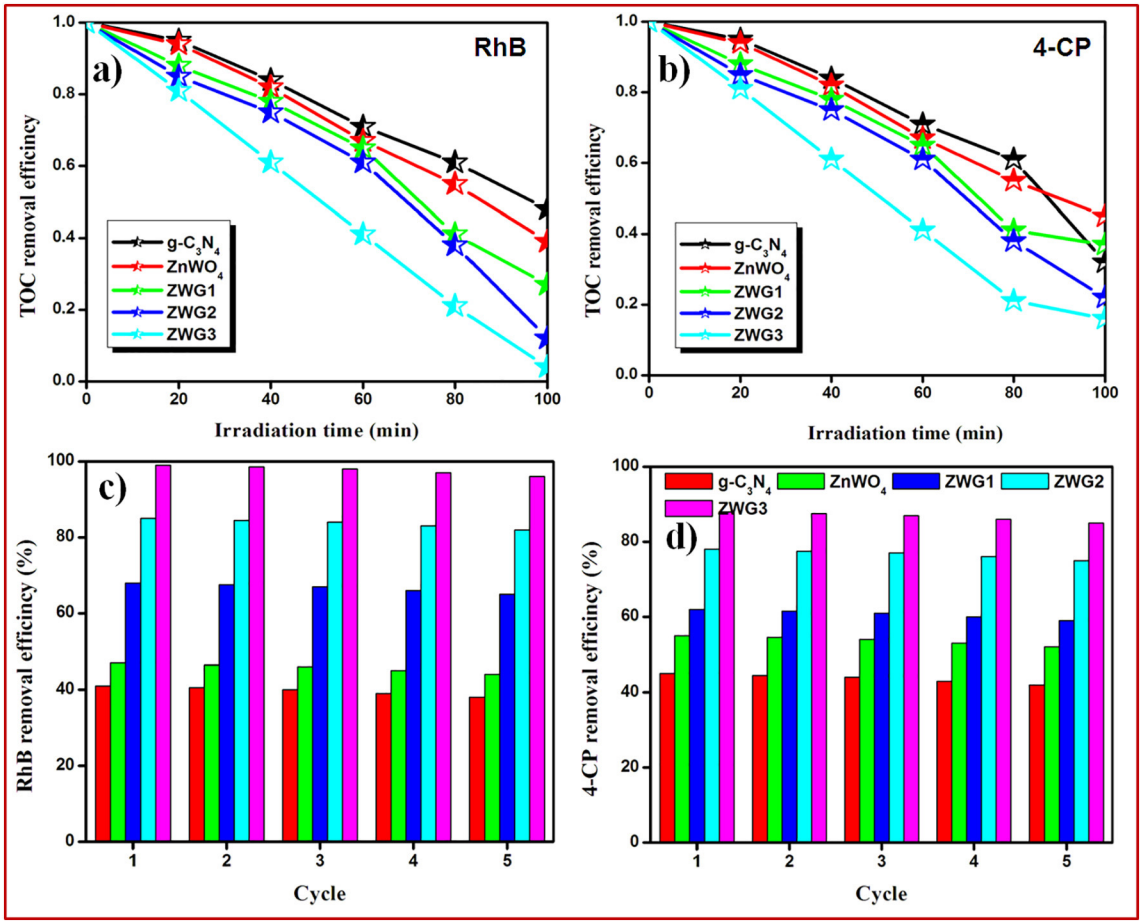


Fig. 9. COD removal efficiency of a) RhB; b) 4-CP for all the catalysts; cycling stability test of c) RhB; d) 4-CP pollutants using all the catalyst samples.

from 0 to 100 min the absorption was started to decreases. The absorption intensity is almost vanishing in the end of 100 min irradiation. The results suggest that the obtained catalysts were highly active in the visible light region to decomposition of toxic pollutants.

3.8.2. Degradation test

Under the same experimental condition the removal efficiency was studied towards RhB and 4-CP pollutants using all the catalysts. Fig. 8(a &b) sows the temporal degradation profile of RhB and 4-CP dyes under stimulated visible source. The composite catalyst show high removal efficiency towards both dyes compared with bare catalyst sample. The optimized $ZnWO_4$/g-C_3N_4 (ZWG3) catalyst highest activity, which degraded ~99% and 78% of the RhB and 4-CP dye molecules by 100 min visible light irradiation. The degradation efficiency is only ~41 and 47% for the pure g-C_3N_4 and $ZnWO_4$ catalysts, respectively (RhB dye). The order of the photocatalytic performance is as follows; ZWG3 > ZWG2 > ZWG1 > $ZnWO_4$ > g-C_3N_4. The improved catalytic activity of the composite catalysts is mainly due to the following reasons (i) rapid generation of electron-hole pair (ii) suppress the recombination rate of electron-hole pairs (iii) high surface area and (iv) huge absorption visible light on the catalyst surface during the photocatalytic reaction.

3.8.3. Kinetic study

The kinetics of MO and RhB photodecomposition on the catalyst surface could be described by the pseudo first-order reaction model ln $(C_0/C) = kt$ where k was the reaction rate constant, C_0 was the concentration of MO and RhB when the absorption–desorption equilibrium has been reached, and C was the actual concentration of MO and RhB at reaction time t [45]. The resultant plot is shown in Fig. 8(c&d). The apparent constant (k) of RhB and 4-CP dyes are 0.0931 min^{-1} and 0.0721 min^{-1}, which is 4.21 times (0.0221 min^{-1}) and 6.4 times (0.0112 min^{-1}) better than bare $ZnWO_4$ catalyst. Based on the photocatalytic results the photocatalytic parameter values are estimated and summarized in Table 1. Among the various composite catalysts, the 3:1 mass ratio of $ZnWO_4$/g-C_3N_4 (ZWG3) catalyst show outstanding degradation efficiency towards RhB and 4-CP dyes. This behavior was further confirmed through the variation in their composites ratio. Further the ratio of g-C_3N_4:$ZnWO_4$ is adjust to 4:1 and 5:1 and denoted as ZWG4 and ZWG5, respectively. The degradation efficiency was found to be 43, 73, 99, 84 and 73 for ZWG1, ZWG2, ZWG3, ZWG4 and ZWG5 catalysts, respectively (Fig. 8e&f). The same trend was also obtained in the 4-CP removal efficiency. Hence, the results suggest that the optimum ratio of 3:1 $ZnWO_4$/g-C_3N_4 (ZWG3) catalyst show outstanding degradation efficiency compared with other composite catalysts.

3.8.4. COD removal test

The high catalytic efficiency of the obtained catalysts was further evaluated through the monitoring COD removal efficiency both dyes and the results are shown in Fig. 9(a&b). The results demonstrate that the maximum decolonization efficiency was achieved by ZWG3 catalysts, it was found to be 96 and 84% for COD removal efficiency of RhB and 4-CP pollutants.

3.8.5. Stability test

The stability test was further carried out to identify the appropriateness of the practical device applications of the current catalysts. Fig. 9(c&d) long term stability test of the catalysts towards RhB and 4-CP dyes under same experimental condition. After five successive runs, no obvious decomposition is detected. After the 5th run a slight loss could be observed in the removal efficiency of both dyes. Thus, it was terminating that the obtained catalysts were demonstrating tremendous stability and it can be useful for photo-electrochemical and waste water treatment applications.

3.8.6. Photocatalytic mechanism

A proposed mechanism for the catalytic degradation of RhB is shown in Fig. 10. In the g-C_3N_4/$ZnWO_4$ heterojunction system, the work function of g-C_3N_4 is higher than that of $ZnWO_4$, which causes the electrons to flow from the $ZnWO_4$ to the g-C_3N_4 until the Fermi levels of the two materials are aligned. As a result, the g-C_3N_4 is negatively charged and the $ZnWO_4$ is positively charged near the heterojunction's surface due to electrostatic induction. After the two phases are in contact and reach electrical equilibrium, the energy bands of g-C_3N_4 bend downward and $ZnWO_4$ bend upward near the interface. Initially, adsorption of RhB dye molecules took place over the surface of the g-C_3N_4/$ZnWO_4$ composite followed by catalytic oxidation as a result of hydroxyl radicals. Surface adsorbed material was preceded for visible light illumination which upon excitation causes the movement of electron from valence to conduction band in step, which trapped over the graphene network and provided a channeling to photo-excited electron, which in turn reduces the chances of e^-/h^+ recombination. Photo trapped electron reacts with surface adsorbed oxygen to produce reactive oxygen species (ROS) in the form of superoxide and peroxide radicals. On the other hand, hydroxyl radicals are generated, which are responsible for oxidative degradation of RhB.

4. Conclusions

In summing up, we have rationally developed a 2D multilayered nanostructure photocatalysts with various compositions of $ZnWO_4$ and g-C_3N_4 by a one step facile hydrothermal route. Numerous characterizations such as XRD, TEM, Raman, UV, PL, BET and EDS have been explored to investigate their structural, morphological and optical properties. XRD and TEM results indicate the reasonable existence of g-C_3N_4 (001)-$ZnWO_4$ (010) interfaces. The incorporated g-C_3N_4 layer has shown a great impact on the structure and properties, including lattice expansion, band-gap narrowing, luminescence enhancement, as well as photocatalytic activity. The effective prevention of electron-hole pair is observed by the photoluminescence emission intensities. A significant reduction of band gap and prevent the recombination of electron-hole pair is the major role to improving the photocatalytic activity. Visible light induced photocatalytic degradation test was carried out for all the synthesized catalysts towards rhodamine B (RhB) and 4-chlorophenol (4-CP) dyes. The results reveal that the hybrid catalyst show outstanding degradation efficiency of 99%, high apparent constant (0.0931 min^{-1}) and long term stability towards RhB dye under visible light irradiation. The role of g-C_3N_4 as the light sensitizer to $ZnWO_4$ is proven to be real and the microscopic mechanisms of charge transfer and separation for the g-C_3N_4–$ZnWO_4$ interface are revealed as well. The present investigation is useful in wider development of new heterojunction photocatalysts and will be of great importance to meet the environmental demands in the near future.

Declaration of competing interest

The authors declare that they have no known competing financial interests or personal relationships that could have appeared to influence the work reported in this paper.

References

[1] A. Fujishima, K. Honda, Electrochemical photolysis of water at a semiconductor electrode, Nature 238 (1972) 37–38.
[2] S. Malato, J. Blanco, C. Richter, M. Maldonado, Optimization of pre-industrial solar photocatalytic mineralization of commercial pesticides: application to pesticide container recycling, Appl. Catal. B Environ. 25 (2000) 31–38.
[3] R. Asahi, T. Morikawa, T. Ohwaki, K. Aoki, Y. Taga, Visible-light photocatalysis in nitrogen-doped titanium oxides, Science 293 (2001) 269–271.
[4] Z. Zou, J. Ye, K. Sayama, H. Arakawa, Direct splitting of water under visible light irradiation with an oxide semiconductor photocatalyst, Nature. 414 (2001) 625–627.
[5] A.A. Khodia, T. Sehili, J.F. Pilichowski, P. Boule, Photocatalytic degradation of 2-

phenylphenol on TiO_2 and ZnO in aqueous suspensions, J. Photochem. Photobiol. A Chem. 141 (2001) 231–239.
[6] M. Rodriguez, V. Sarria, S. Esplugas, C. Pulgarin, Photo-Fenton treatment of a biorecalcitrant wastewater generated in textile activities: biodegradability of the photo-treated solution, J. Photochem. Photobiol. A Chem. 151 (2002) 129–135.
[7] A. Kudo, Y. Miseki, Heterogeneous photocatalyst materials for water splitting, Chem. Soc. Rev. 38 (2009) 253–278.
[8] R. Wang, K. Hashimoto, A. Fujishima, M. Chikuni, E. Kojima, A. Kitamura, M. Shimohigoshi, T. Watanabe, Light-induced amphiphilic surfaces, Nature 388 (1997) 431–432.
[9] C.Y. Wang, H.M. Shang, T. Ying, T.S. Yuan, G.W. Zhang, Properties and morphology of CdS compounded TiO_2 visible-light photocatalytic nanofilms coated on glass surface, Sep. Purif. Technol. 32 (2003) 357–362.
[10] M. Anpo, M. Takeuchi, The design and development of highly reactive titanium oxide photocatalysts operating under visible light irradiation, J. Catal. 216 (2003) 505–516.
[11] H. Yamashita, M. Harada, J. Misake, M. Takeuchi, B. Neppolian, M. Anpo, Photocatalytic degradation of organic compounds diluted in water using visible light-responsive metal ion- implanted TiO_2 catalysts: Fe ion-implanted TiO_2, Catal. Today 84 (2003) 191–196.
[12] M.M. Khin, A.S. Nair, V.J. Babu, R. Murugan, S. Ramakrishna, A review on nano-materials for environmental remediation, Energy Environ. Sci. 5 (2012) 8075–8109.
[13] P. Dong, G. Hou, X. Xi, R. Shao, F. Dong, WO3-based photocatalysts: morphology control, activity enhancement and multifunctional applications, Environ. Sci. Nano 4 (2017) 539–557.
[14] S.H. Yu, B. Liu, M.S. Mo, J.H. Huang, X.M. Liu, Y.T. Qian, General synthesis of single-crystal tungstate nanorods/nanowires: a facile, low-temperature solution approach, Adv. Funct. Mater. 13 (2003) 639–647.
[15] X.F. Shi, J.G. Li, Q. Zhu, X.D. Li, X.D. Sun, Hydrothermal assisted synthesis and photoluminescence of $(Y_{1-x}Eu_x)_2WO_6$ red phosphors, J. Alloys Compd. 695 (2017) 1984–1992.
[16] X.P. Chen, F. Xiao, S. Ye, X.Y. Huang, G.P. Dong, Q.Y. Zhang, $ZnWO_4$:Eu^{3+} nanorods: a potential tunable white light-emitting phosphors, J. Alloys Compd. 509 (2011) 1355–1359.
[17] P.F.S. Pereira, A.F. Gouveia, M. Assis, R.C.D. Oliveira, I.M. Pinatti, M. Penha, R.F. Goncalves, L. Gracia, J. Andresd, E. Longoa, $ZnWO_4$ nanocrystals: synthesis, morphology, photoluminescence and photocatalytic properties, Phys. Chem. Chem. Phys. 20 (2018) 1923–1937.
[18] X. Huang, X. Qi, F. Boey, H. Zhang, Graphene-based composites, Chem. Soc. Rev. 41 (2012) 666–686.
[19] Q.Z. Wang, L.H. Zheng, Y. Bai, J.J. Zhao, F.P. Wang, R. Zhang, H.H. Huang, B.T. Su, $Zn_3(OH)_2V_2O_{7\cdot2}H_2O$/g-$C_3N_4$: a novel composite for efficient photodegradation of methylene blue under visible-light irradiation, Appl. Surf. Sci. 347 (2015) 602–609.
[20] S. Zhan, F. Zhou, N.B. Huang, Y.F. Yin, M. Wang, Y.F. Yang, Y.J. Liu, Sonochemical synthesis of $Zn_3V_2O_7(OH)_2(H_2O)_2$ and g-C_3N_4/$Zn_3V_2O_7(OH)_2(H_2O)_2$ with high photocatalytic activities, J. Mol. Catal. A Chem. 401 (2015) 41–47.
[21] S.Z. Wu, K. Li, W.D. Zhang, On the heterostructured photocatalysts Ag_3VO_4/g-C_3N_4 with enhanced visible light photocatalytic activity, Appl. Surf. Sci. 324 (2015) 324–331.
[22] N. Tian, H.W. Huang, Y.X. Guo, Y. He, Y.H. Zhang, A g-C_3N_4/$Bi_2O_2CO_3$ composite with high visible-light-driven photocatalytic activity for rhodamine B degradation, Appl. Surf. Sci. 322 (2014) 249–254.
[23] F. Chang, J. Zhang, Y.C. Xie, J. Chen, C.L. Li, J. Wang, J.R. Luo, B.Q. Deng, X.F. Hu, Fabrication, charaterization, and photocatalytic performance of exfoliated g-C_3N_4–TiO_2 hybrids, Appl. Surf. Sci. 311 (2014) 574–581.
[24] S.Z. Hu, L. Ma, J.G. You, F.Y. Li, Z.P. Fan, G. Lu, D. Liu, J.Z. Gui, Enhanced visible light photocatalytic performance of g-C_3N_4 photocatalysts co-doped with iron and phosphorus, Appl. Surf. Sci. 311 (2014) 164–171.
[25] Y. Xu, S.P. Gao, Band gap of C_3N_4 in the GW approximation, Int. J. Hydrog. Energy 37 (2012) 11072–11080.
[26] W. Wang, J. Shen, N. Li, M. Ye, Synthesis of novel photocatalytic RGO-$ZnWO_4$ nanocomposites with visible light photoactivity, Mater. Lett. 106 (2013) 284–286.
[27] M.M.J. Sadiq, U.S. Shenoy, D.K. Bhat, Novel RGO-$ZnWO_4$-Fe_3O_4 nanocomposite as high performance visible light photocatalyst, RSC Adv. 6 (2016) 61821–61829.
[28] M.M.J. Sadiq, A.S. Nesaraj, Soft chemical synthesis and characterization of $BaWO_4$ nanoparticles for photocatalytic removal of Rhodamine B present in water sample, J. Nanostruct. Chem. 5 (2015) 45–54.
[29] M.J. Sadiq Mohamed, K. Bhat Denthaje, Novel RGO-$ZnWO_4$-Fe_3O_4 nanocomposite as an efficient catalyst for rapid reduction of 4-nitrophenol to 4-aminophenol, Ind. Eng. Chem. Res. 55 (2016) 7267–7272.
[30] Liming Sun, Xian Zhao, Chun-Jiang Jia, Yixuan Zhou, Xiufeng Cheng, Li Pan, Li Liu, Weiliu Fan, Enhanced visible-light photocatalytic activity of g-C_3N_4–$ZnWO_4$ by fabricating a heterojunction: investigation based on experimental and theoretical studies, J. Mater. Chem. 22 (2012) 23428.
[31] S. Prabhu, M. Pudukudy, S. Harish, M. Navaneethan, S. Sohila, K. Murugesan, R. Ramesh, Facile construction of djembe-like ZnO and its composite with g-C_3N_4 as a visible-light- driven heterojunction photocatalyst for the degradation of organic dyes, Mater. Sci. Semicond. Process. 106 (2020) 10454.
[32] M. Arami, N.Y. Limaee, N.M. Mahmoodi, N. Salman, Equilibrium and kinetics studies for the adsorption of direct and acid dyes from aqueous solution by soy meal hull, J. Hazard. Mater. 135 (2006) 11–19.
[33] I.K. Konstantinou, T.A. Albanis, TiO_2-assisted photocatalytic degradation of azo dyes in aqueous solution: kinetic and mechanistic investigations: a review, Appl. Catal. B Environ. 49 (2014) 1–14.
[34] H.N. Che, G.B. Che, H.J. Dong, W. Hu, H. Hu, C.B. Liu, C. Liu, Fabrication of Z-scheme Bi_3O_4Cl/g-C_3N_4 2D/2D heterojunctions with enhanced interfacial charge separation and photocatalytic degradation various organic pollutants activity, Appl. Surf. Sci. 455 (2018) 705–716.
[35] R. Shi, Y.J. Wang, D. Li, J. Xu, Y.F. Zhu, Synthesis of $ZnWO_4$ nanorods with [100] orientation and enhanced photocatalytic properties, Appl. Catal. B Environ. 100 (2010) 173–178.
[36] Xiufang He, Zhansheng Wu, Yongtao Xue, Zhenzhen Gao, Xia Yang, Fabrication of interlayer β-CD/g-C_3N_4@MoS_2 for highly enhanced photodegradation of glyphosate under simulated sunlight irradiation, RSC Adv. 9 (2019) 4635–4643.
[37] J. Theo Kloprogge, Matt L. Weier, Loc V. Duong, Ray L. Frost, Microwave-assisted synthesis and characterisation of divalent metal tungstate nanocrystalline minerals: ferberite, hubnerite, sanmartinite, scheelite and stolzite, Mater. Chem. Phys. 885 (2004) 438–443.
[38] V.V. Fomichev, O.I. Kondratov, Vibrational spectra of compounds with the wolframite structure, Spectrochim. Acta A 50 (1994) 1113–1120.
[39] M. Parthibavarman, S. Sathishkumar, S. Prabhakaran, M. Jayashree, R. BoopathiRaja, High visible light-driven photocatalytic activity of large surface area Cu doped SnO_2 nanorods synthesized by novel one-step microwave irradiation method, J. Iran. Chem. Soc. 15 (2018) 2789–2801.
[40] M. Parthibavarman, M. Karthik, P. Sathishkumar, R. Poonguzhali, Rapid synthesis of novel Cr-doped WO_3 nanorods: an efficient electrochemical and photocatalytic performance, J. Iran. Chem. Soc. 15 (2018) 1419–1430.
[41] R. BoopathiRaja, M. Parthibavarman, A. Nishara Begum, Hydrothermal induced novel $CuCo_2O_4$ electrode for high performance supercapacitor applications, Vacuum 165 (2019) 96–104.
[42] R. BoopathiRaja, M. Parthibavarman, Hetero-structure arrays of $MnCo_2O_4$ nano-flakes@ nanowires grown on Ni foam: design, fabrication and applications in electrochemical energy storage, J. Alloys Compd. 811 (2019) 152084.
[43] S.W. Cao, Y.P. Yuan, J. Barber, S.C.J. Loo, C. Xue, Noble-metal-free g-C_3N_4/Ni$(dmgH)_2$ composite for efficient photocatalytic hydrogen evolution under visible light irradiation, Appl. Surf. Sci. 319 (2014) 344–349.
[44] S.W. Cao, J.X. Low, J.G. Yu, M. Jaroniec, Polymeric photocatalysts based on graphitic carbon nitride, Adv. Mater. 27 (2015) 2150–2176.
[45] F. Chen, Q. Yang, Y. Wang, J.W. Zhao, D.B. Wang, X.M. Li, Z. Guo, H. Wang, Y.C. Deng, C.G. Niu, G.M. Zeng, Novel ternary heterojunction photcocatalyst of Ag nanoparticles and g-C_3N_4 nanosheets co-modified $BiVO_4$ for wider spectrum visible-light photocatalytic degradation of refractory pollutant, Appl. Catal. B Environ. 205 (2017) 133–147.